An Optimized Digital Synchronous Rectification Scheme Based on Time-Domain Model of Resonant CLLC Circuit

Bodong Li, *Student Member, IEEE*, Min Chen, *Member, IEEE*, Xiaoqing Wang, *Student Member, IEEE*, Ning Chen, *Student Member, IEEE*, Xinnan Sun, and Dongbo Zhang

***Abstract*—Uncontrolled rectification on the secondary side of the resonant CLLC circuit causes a large amount of conduction loss. Accurate synchronous rectification (SR) can reduce conduction loss by replacing rectifier diodes with mosfets' channels exactly. The accuracy of the SR signals depends on the determination of the zero-crossing points of the secondary side resonant current. In this article, an accurate time-domain model is introduced for the resonant CLLC circuit to obtain these zero-crossing points. This modeling method is more accurate than first harmonic approximation and requires less computational effort than extended harmonics approximation. Compared with previous time-domain modeling methods, the proposed time-domain model gives detailed circuit state expressions and covers the entire circuit operating states. Relying on the accurate circuit model, the SR scheme proposed in this article can adaptively generate SR signals in different frequency ranges and has the ability to switch modes smoothly. And this method can be used for the later efficiency optimization of CLLC converters that do not originally have SR function, only through the control program update. Moreover, the robustness of the proposed SR method is analyzed, and the proposed concept is verified through a 3-kW resonant CLLC prototype.**

***Index Terms*—High efficiency, resonant CLLC circuit, synchronous rectification (SR), time-domain model.**

NOMENCLATURE

LRFM	Lower resonant frequency mode.
RFM	Resonant frequency mode.
URFM	Upper resonant frequency mode.
α_n, β_n	Undetermined parameters in URFM.
φ	SR angle.
φ_{Aa}	SR angle in DSP table.
φ_{Lower}	SR angle in LRFM.
φ_{Upper}	SR angle in URFM.
ω	Switching angular frequency.
ω_{an}	Normalized ratio similar to ω_n in *Stage a*.
ω_b	Normalized ratio similar to ω_n in *Stage b*.
ω_m	Normalized ratio similar to ω_n.
ω_n	Normalized switching angular frequency.
ω_r	Resonance angular frequency.
A_{an}	Undetermined parameters in *Stage a*.
A_{bn}	Undetermined parameters in *Stage b*.
C_r	Equivalent resonant capacitor.
C_{rp}	Resonant capacitor on the primary side.
C_{rs}	Resonant capacitor on the secondary side.
C_P	Input capacitor on the primary side.
C_S	Output capacitor on the secondary side.
$\mathrm{D}_{\mathrm{S}n}$	Inverse parallel diode of S_n.
f_m	Normalized ratio similar to f_n.
f_n	Normalized switching frequency.
f_r	Resonance frequency.
f_s	Switching frequency.
f_{sa}	Switching frequency in DSP table.
$\dot{I}_2$	The first harmonic component of i_2.
i_1	Input current in time-domain model.
i_2	Output current in time-domain model.
i_d	The difference between i_1 and i_2.
i_{Lm}	Magnetizing inductor current on the primary side.
i_{Lrp}	Resonant current on the primary side.
i_{Lrs}	Resonant current on the secondary side.
i_m	Magnetizing inductor current in time-domain model.
i_s	The sum between i_1 and i_2.
$i_{SD.n}$	The current from source to drain of MOSFET.
k	Ratio of L_m to L_r.
L_m	Magnetizing inductor on the primary side.
L_r	Equivalent resonant inductor.
L_{rp}	Resonant inductor on the primary side.
L_{rs}	Resonant inductor on the secondary side.
M	Voltage gain.
n	Transformer ratio.
P	Converter transmission power.
Q	Quality factor.
R_{eq}	Equivalent resistance.
S_n	Switching device.
SR_{on}	The lag time of the SR signal turn-ON.
SR_{off}	The lag time of the SR signal turn-OFF.
T_S	Switching cycle.
t_0	The beginning of a switching cycle.

Manuscript received August 18, 2020; revised November 6, 2020; accepted December 6, 2020. Date of publication December 14, 2020; date of current version June 1, 2021. This work was supported by the National Key R&D Program of China under Grant 2018YFB1503002. Recommended for publication by Associate Editor J. Acero. *(Corresponding author: Min Chen.)*

The authors are with the Department of Applied Electronics, Zhejiang University, Hangzhou 310027, China (e-mail: bodong_li@zju.edu.cn; calim@zju.edu.cn; 11710013@zju.edu.cn; 3140103335@zju.edu.cn; 3150103575@zju.edu.cn; dongbo_zhang@zju.edu.cn).

Color versions of one or more figures in this article are available at https://doi.org/10.1109/TPEL.2020.3044297.

Digital Object Identifier 10.1109/TPEL.2020.3044297

t_{Ts}	The ending of a switching cycle.
t_{s0}, t'_{s0}	The time when i_{Lrs} crosses zero.
t_{p0}	The time when i_{Lrp} crosses zero.
$t_{Ts/2}$	The midpoint of a switching cycle.
$V_{GS.n}$	Drive signals on the primary side.
$V_{GS.L.n}$	SR drive signals in LRFM.
$V_{GS.U.n}$	SR drive signals in URFM.
V_P	Input voltage on the primary side.
V_S	Output voltage on the secondary side.
V_1	The conversion results of V_P in time-domain model.
V_2	The conversion results of V_S in time-domain model.
$\dot{V}_{AB.F}$	The first harmonic component of v_{AB}.
V_o	Converter output voltage.
V_{oA}	Converter output voltage in DSP table.
v_{AB}	The voltage between A and B.
v_1	Input voltage in time-domain model.
v_2	Output voltage in time-domain model.
v_{L1}, v_{L2}	Resonant inductor voltage in time-domain model.
v_{C1}, v_{C2}	Resonant capacitor voltage in time-domain model.
v_{Cd}	The difference between v_{C1} and v_{C2}.
v_{Cs}	The sum between v_{C1} and v_{C2}.
v_{DSP}	The voltage across the primary MOSFET.
v_{DSS}	The voltage across the secondary MOSFET.

I. Introduction

ISOLATED bidirectional dc–dc converters are available in a variety of applications, such as microgrid, on-board-charger (OBC) in electric vehicle, energy storage systems, power electronic transformer, and so on [1]–[4]. At present, dual-active-bridge (DAB) and resonant CLLC circuit topology are widely concerned in the research of isolated bidirectional dc–dc converters due to their common advantages such as high efficiency, high power density, wide gain range, and zero-voltage-switching (ZVS) feature [5]–[8].

Compared with the resonant CLLC circuit, the research on the DAB circuit is relatively early and comparatively mature. However, due to the increase of circulating current and the loss of the ZVS feature, the efficiency of the DAB circuit with single phase-shift-control is significantly reduced under the unmatched voltage between input and output as well as light load situations [9]. To solve these problems, control methods in [10]–[12] increase the degrees of freedom based on single-phase-shift-control, realizing the minimum circulating current and ZVS feature in the whole load range. Nevertheless, the control of multidegrees of freedom increases the complexity of the control system, and DAB is challenging to work at a higher switching frequency to improve the power density. DAB still has the defect of MOSFETs switching when the current reaches the peak, which causes a tremendous turn-OFF loss. In contrast, the resonant CLLC circuit topology makes it easier to implement the ZVS feature in full range. It has a relatively small turn-OFF loss [13], [14]. Therefore, the resonant CLLC circuit is widely studied as an alternative circuit to DAB currently.

A series of studies [15]–[20] have made some progress in topological structure, model establishment, parameter design, and control optimization of the resonant CLLC circuit. It is well known that the bidirectional CLLC circuit is evolved from the single-direction LLC circuit. LLC circuit is widely used in industry due to high efficiency and high power density. However, compared with the CLLC circuit, the LLC circuit cannot achieve the boost function when operating in backward mode [15]. In [16], the forward and backward voltage gains of the LLC-type resonant network in frequency-domain were analyzed. The method of changing the structure of the resonant network to increase the maximum voltage gain for the backward working situation was proposed. Research in [17] added just one capacitor to the secondary side based on the LLC topology and proposed a new type of bidirectional asymmetric CLLC-type resonant network. This topology achieves a wide range of gain adjustments, with the ZVS feature in the full range of the primary side satisfying bidirectional power flow. However, the asymmetric CLLC-type resonant network makes the gain characteristics of the forward and backward modes of operation substantially different, which is not conducive to application design. To simplify the resonant network's design process, Jung *et al.* [18] proposed a symmetric CLLC-type resonant network and analyzed the relationship between the gain curve and frequency variation by first harmonic approximation (FHA). Based on the FHA method, He and Khaligh [19] gave the expression of the gain and normalized frequency of the resonant CLLC circuit. Furthermore, the research in [20] introduced a comprehensive design process of the CLLC converter, simplifying the design of the multiparameter CLLC topology.

To sum up, the resonant CLLC converter has the excellent characteristic of switching loss, and it can be devoted to reducing the volume of passive components at high switching frequency. However, the secondary side bridge operates in rectification mode. Each MOSFET body diode on the secondary side has a sizeable ON-state voltage drop, especially for SiC MOSFET, which will significantly reduce the efficiency of the CLLC converter [21]. Synchronous rectification (SR) can effectively solve this problem and substantially improve the converter's efficiency.

The basic idea of SR is to use the MOSFETs' channels to replace the body diodes for rectification. During SR process, the drive signals of the MOSFETs are determined based on the ON/OFF time of the body diodes. The working states of the body diodes can be obtained by the methods shown in Table I. The working principles of these SR methods are shown as follows.

TABLE I
COMPARISON TABLE OF THREE SR METHODS

Items	Voltage Detection	Current Detection	Calculation Prediction
Typical examples	[22]	[23]	[24]-[26]
Accuracy	★★	★★★	★★
Difficulty of realization	★★★	★★	★★
Efficiency	★★	★	★★★
Power density	★★	★	★★★
Versatility	★	★★★	★★★
Economy	★★	★	★★★

*"★" is the unit of quantization.

1) *Voltage Detection*: This method achieves SR by detecting the voltage drops of body diodes since the magnitude of this voltage will change depending on whether there is a reverse current [22]. However, the magnitude of this voltage is relatively small compared to the output voltage. The detection accuracy for this voltage is difficult to guarantee. Besides, the detection result of this voltage is also easily affected by the parasitic parameters in the circuit.
2) *Current Detection*: Through the current detection circuit with current transducer, the current change through the body diodes can be accurately obtained. The polarity change of this current can be directly transmitted to the drive circuit. This SR scheme based on current detection has strong versatility and anti-interference ability [23]. However, the current detection circuit has a large volume and weight, which will reduce power density and increase the converter's cost. Chen *et al.* [8] proposed a SR scheme based on resonant inductor voltage sensing. According to the principle that the resonant current is proportional to the integral of the inductor voltage in CLLC circuit, the information of the resonant current is obtained by the voltage detection circuit and the integral circuit. This scheme reduces the size and cost of the detection circuit compared to the scheme that directly detects the inductor current. However, the additional integration circuit will increase the sampling delay, and there is a risk of false triggering of the SR signal when the secondary side resonant current is intermittent.
3) *Calculation Prediction*: Through the calculation and analysis of the circuit model, the digital controller can calculate the turn-ON and turn-OFF time of the MOSFET body diodes, and generate the corresponding SR signals [24]–[26]. The method of digital SR does not require additional detection circuits, and the operating efficiency is high. However, the accuracy of SR depends on the accuracy of the circuit model and is limited by the computing capability of the controller.

In conclusion, the comparison results of three SR methods are shown in Table I. The method of voltage detection is limited by the application scenario. Although the method of current detection is versatile, it increases the size and cost. With the enhancement of the controller's computing capability, the method of calculation prediction based on the accurate circuit model reduces the cost while ensuring accurate performance, which has received extensive attention in recent years.

Gao *et al.* [24] proposed a phase-shift-based SR scheme without additional detection devices for CLLC resonant converters. However, the phase-shift of the SR of the CLLC circuit is related to the multiple circuit states such as the input/output voltage, switching frequency, and transmission power. The specific analysis of these issues lacks in this text. The research in [25] showed an SR control model based on FHA, which will be inaccurate when deviating from the resonant frequency. Inaccurate SR may cause circulating current to affect efficiency. Subsequently, the work in [26] proposed an SR method based on extended harmonics approximation (EHA), which achieves a better SR effect. Nevertheless, analysis of other odd-order harmonics increases the amount of computation, and the control strategy is defective in this article when the switching frequency is less than the resonant frequency.

As mentioned above, the core issue of the calculation prediction scheme is the accurate circuit model. For resonant topology with a wide range of switching frequency variations, FHA typically does not provide sufficient accuracy for design and analysis [27]. The establishment of the EHA model requires a vast amount of calculation and is challenging to promote. Here are some other model building methods worth learning, which are compared in Table II. The simulation analysis method traverses different parameters through the simulation software's built-in algorithm to obtain the working states of the circuit. Due to the massive workload, it is generally only used as a supplement to other analysis methods. Zhao *et al.* [28] proposed an artificial intelligence algorithm based on the optimal design methodology of CLLC resonant converters. Afterward, the research in [29] showed a time-domain model of resonant CLLC converters for faster parameter scanning, compared to MATLAB/Simulink, SIMPLIS, and PLECS simulation methods. However, these methods do not give detailed circuit state expressions and cover the entire circuit operating states. In [27], a general time-domain model of the dual-bridge series resonant converter was created, giving detailed circuit state expressions of the series resonant converter. Compared with the series resonant circuit, the resonant network of the CLLC circuit has multiple resonant components. And in order not to affect the normal operation of the circuit, SR control requires high accuracy of the circuit time-domain model. It is even more challenging to calculate the operating states for the resonant CLLC circuit.

In order to describe the accurate circuit working states of the CLLC circuit, an establishment process of a time-domain model is introduced. This article analyzes the relationship in detail between the three different working modes: lower resonant frequency mode (LRFM), upper resonant frequency mode (URFM), and resonant frequency mode (RFM). Furthermore, the phase shift angle of the primary and secondary sides is selected as the state variable for calculation, simplifying the calculation process. Combining the physical meaning and the mathematical equation reduction method, the simplified time-domain expressions of resonant CLLC circuit under all working conditions are obtained. Subsequently, an optimized digital SR scheme based on the time-domain model applied to the CLLC topology is proposed. Under the premise of ensuring accuracy, it improves the design and application efficiency of the SR control strategy as much as possible. It realizes SR of the entire frequency range, significantly improving the efficiency of the CLLC converters.

This article is organized as follows. In Section I, the modeling methods and the SR schemes of the resonant CLLC circuit have been reviewed and summarized in detail. The existing FHA and EHA modeling methods with the corresponding SR schemes have compromise in accuracy and computational complexity. Therefore, it has important practical significance to introduce the time-domain modeling method that is currently used in low-order circuits (such as series resonant circuits) into high-order CLLC circuits. Section II describes the circuit states of the

TABLE II
COMPARISON TABLE OF MODELING METHODS

Items	FHA	EHA	Simulation	Artificial intelligence algorithm	Time-domain	
					Iteration	Expression
Ref	[24], [25]	[26]	-	[28]	[29]	[27]
Accuracy	★	★★	★★★	★★★	★★★	★★★
Simplicity	★★	★	★★★	★	★	★
Efficiency	★★★	★★	★	★	★★	★★★
Workload	★	★★	★★★	★★★	★★★	★★★
Versatility	★	★★	★	★★	★★	★★★

*"★" is the unit of quantization;
**Simplicity represents the difficulty of modeling;
***Efficiency represents the calculation speed of the model;
****Workload represents the workload of analysis using existing models.

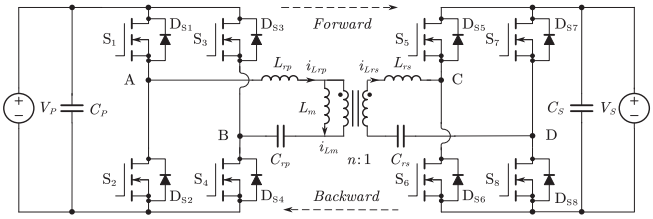

Fig. 1. Circuit topology of the CLLC resonant converter.

resonant CLLC circuit under different switching frequencies and analyzes the influence of SR signal accuracy on circuit operation. Section III builds the time-domain model and obtains accurate circuit state expressions through simplification and gives calculation method of SR angle in different frequency ranges. The sensitivity analysis of the SR angle to resonant inductor and capacitor is carried out to prove the robustness of the proposed SR scheme. Section IV details the working principle and implementation process of the proposed SR method. Next, the proposed control scheme is verified by experiment results presented in Section V. Finally, Section VI concludes this article.

II. ANALYSIS OF RESONANT CLLC TOPOLOGY

The full range of SR method relies on a detailed analysis of the circuit states of different operating modes. The bidirectional resonant CLLC circuit is evolved from the traditional resonant *LLC* circuit. By adding an *LC* resonant network symmetrical to the primary side of the transformer into the secondary side, the bidirectional CLLC circuit can be approximated as a resonant *LLC* circuit, whether working in forward or backward mode. It can meet the buck and boost requirements in both directions. Meanwhile, the bidirectional resonant CLLC circuit also inherits the resonant LLC circuit's control and analysis method.

As shown in Fig. 1, the bidirectional resonant CLLC circuit is mainly composed of three parts: two bridges of switching devices and a symmetrical resonant network containing a high-frequency transformer. To realize the bidirectional power transmission, $S_1 \sim S_8$ use wholly controlled devices, mainly MOSFETs, $D_{S1} \sim D_{S8}$ are the inverse parallel diodes of $S_1 \sim S_8$. L_{rp} and C_{rp} represent the resonant inductor and resonant capacitor on the primary side, respectively, L_{rs} and C_{rs} represent the resonant inductor and resonant capacitor on the secondary side, respectively, and L_m represents the magnetizing inductor of transformer on the primary side. The bidirectional resonant CLLC circuit generally uses variable frequency control. The MOSFETs on the primary side receive the drive signals with the duty cycle of 0.5 in the case of working forward, and uncontrolled rectification is used on the secondary side.

The bidirectional resonant CLLC circuit follows the variable frequency control method commonly used in resonant circuits. When the switching frequency changes, the values of the impedance of the passive components in the circuit change accordingly. Under certain input conditions, due to the voltage division's principle, the output voltage, current, and power are controlled by changing switching frequency. In the bidirectional resonant CLLC circuit, when the switching frequency f_s changes, working modes can be divided into three types according to frequency band: LRFM ($f_s < f_r$), URFM ($f_s > f_r$), and RFM ($f_s = f_r$), where f_r is the resonance frequency.

To simplify the analysis process, assuming that each component is ideal in steady state and the dead time is ignored, each working process is analyzed below.

1) Analysis in LRFM ($f_s < f_r$)

Fig. 2 shows the CLLC circuit's waveforms working in the LRFM ($f_s < f_r$), $t_0 \sim t_{Ts}$ represents a complete switching cycle. The circuit waveforms have the characteristics of half-wave symmetry, so only the working process of the first half switching cycle needs to be considered. In the LRFM, the first half switching cycle can be divided into two stages: *Stage a* and *Stage b*.

By extracting the components involved in the two stages of *Stage a* and *Stage b*, the equivalent circuit diagrams of the two stages can be obtained, as shown in Fig. 3. The working process will be described below.

Stage a ($t_0 \sim t_{s0}$): At the instant of time t_0 as shown in Fig. 3(a), the switches S_2 and S_3 turn OFF, the primary resonant current $i_{Lrp} < 0$ through the inverse parallel diodes D_{S1} and D_{S4} of the switches S_1 and S_4. Then, the switches S_1 and S_4 turn ON, the CLLC circuit realizes ZVS while the voltage between two points A and B is constant V_P. During the period from t_0

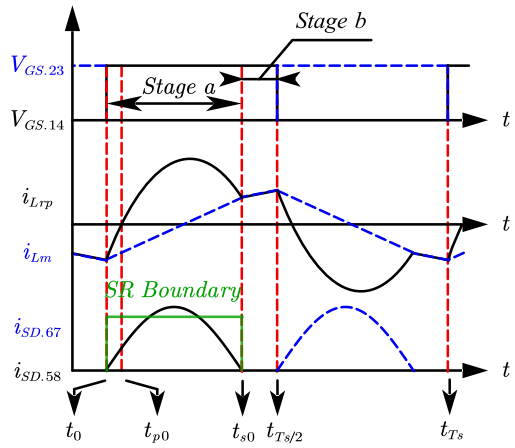

Fig. 2. Waveforms of LRFM.

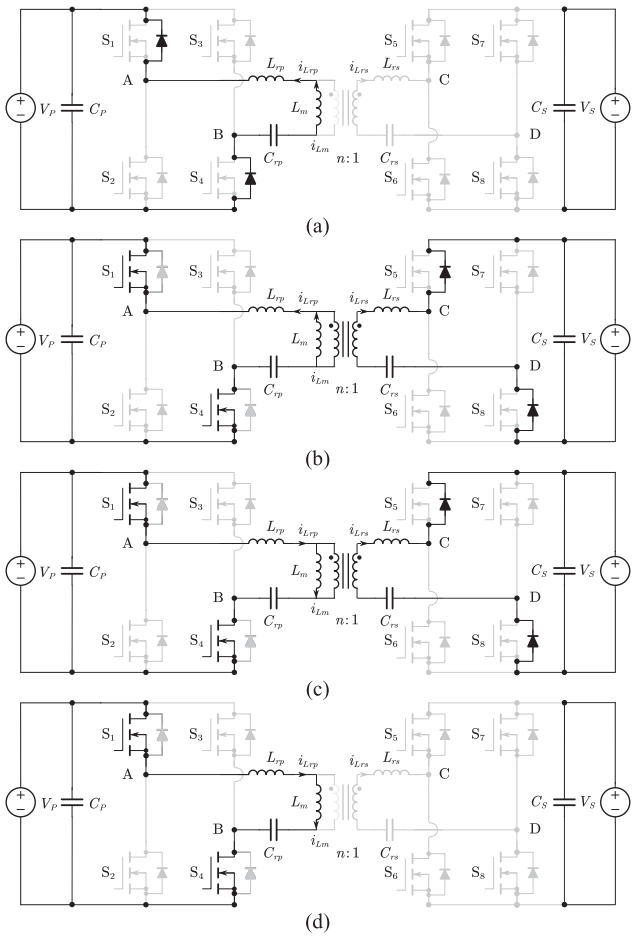

Fig. 3. Equivalent circuit diagram of LRFM. (a) At the instant of time t_0. (b) Time period t_0 to t_{p0}. (c) Time period t_{p0} to t_{s0}. (d) Time period t_{s0} to $t_{Ts/2}$.

to t_{s0}, i_{Lrp} rises faster than the magnetizing inductor current i_{Lm}, which generates a positive resonant current i_{Lrs} on the secondary side, and the inverse parallel diodes D_{S5} and D_{S8} naturally turn ON, the voltage between two points C and D is constant V_S. At t_{p0}, i_{Lrp} crosses zero and divides the circuit

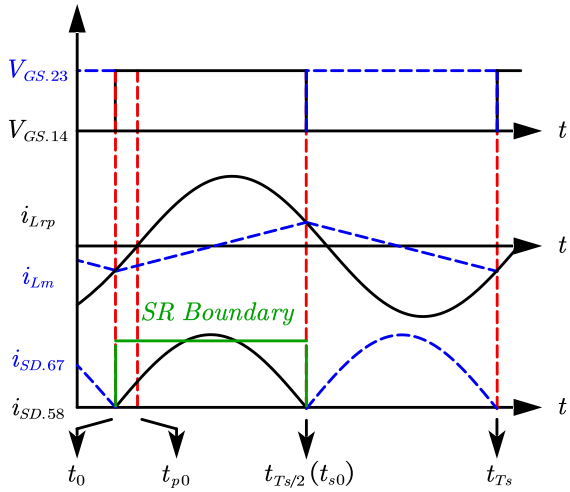

Fig. 4. Waveforms of RFM.

state into two types, as shown in Fig. 3(b) and (c). S_1 and S_4 remain ON-state and the structure of the equivalent circuit is not changed.

Stage b ($t_{s0} \sim t_{Ts/2}$): At t_{s0}, due to the resonant network effect, i_{Lrp} is reduced to be equal to i_{Lm}, the resonant current i_{Lrs} on the secondary side is also reduced to 0, and the diodes D_{S5} and D_{S8} turn OFF naturally. From t_{s0} to $t_{Ts/2}$, i_{Lrs} is kept at zero until the next switching action, and the circuits of primary and secondary sides work separately.

The SR boundary indicates the ON and OFF of the SR drive. The SR signal within this range will not affect the normal operation of the circuit.

2) Analysis in RFM ($f_s = f_r$)

As shown in Fig. 4, the bidirectional resonant CLLC circuit operates in the RFM ($f_s = f_r$). Compared with the LRFM, the diodes rectifier on the secondary side in the RFM is in critical conduction mode (CRM). There is no *Stage b*, and the entire working process is the same as *Stage a* in the LRFM. In particular, when the switching devices on the primary side switch the ON/OFF state, the diodes on the secondary side switch at the same time.

3) Analysis in URFM ($f_s > f_r$)

As shown in Fig. 5, compared with the LRFM, when the switching devices on the primary side switch the ON/OFF state, the resonant current i_{Lrs} on the secondary side has not reached 0. At this time, the uncontrolled rectifier diodes on the secondary side are the inverse parallel diodes D_{S6} and D_{S7}, and the equivalent circuit diagram is shown in Fig. 6. From t_0 to t_{s0}, the voltage between two points C and D is constant $-V_S$. From t_{s0} to $t_{Ts/2}$, the working process is the same as *Stage a* in the LRFM.

In Fig. 7, drive and SR represent the primary drive signal and SR signal in the secondary side, respectively, and i_{Lrs} represents the secondary resonant current. Fig. 7(a) shows the critical point of the SR drive signal SR_{on} and SR_{off} on the time axis; Fig. 7(b) and (c) respectively show the abnormal state of the circuit when

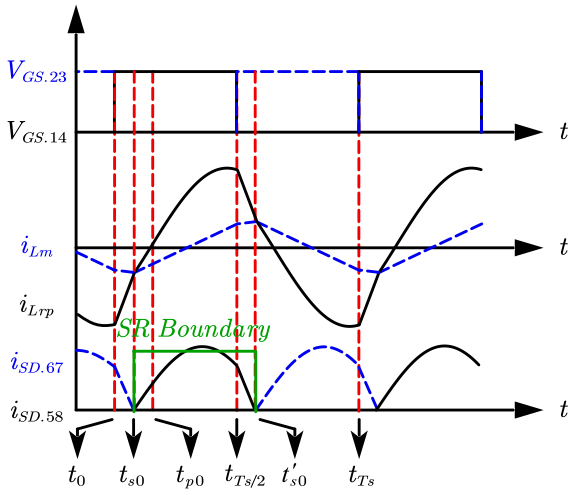

Fig. 5. Waveforms of URFM.

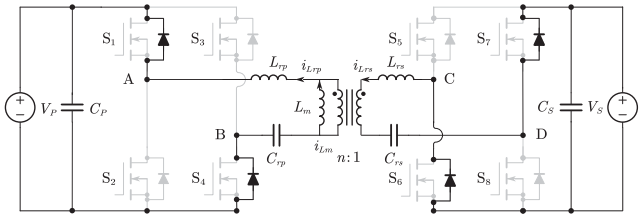

Fig. 6. Equivalent circuit diagram of URFM from t_0 to t_{s0}.

the SR drive signals turn ON too early and turn OFF too late; the SR signal in Fig. 7(d) adds a certain dead time on the basis of Fig. 7(a) to prevent the occurrence of the situations shown in Fig. 7(b) and (c). Compared with the SR signal of Fig. 7(a), these dead times do not affect the normal operation of the circuit. In addition, they will not cause large losses, for the value of the secondary side resonant current i_{Lrs} is small during the dead time.

III. Time-Domain Model of the Resonant CLLC Topology

The FHA model only considers the first harmonic and has low accuracy. The EHA model considers other odd-order harmonics, but it is computationally expensive. In addition to the FHA and EHA mentioned above, the circuit modeling methods also include the time-domain model analysis method and simulation analysis method. The simulation analysis method builds a model in the simulation software and sets the parameters therein according to the variables. Simulation software relies on iterative calculations to obtain convergence points. The statistical analysis of the obtained data is needed to get the relationship between the variables, so the simulation analysis method is accurate but requires extensive work.

The basic principle of the time-domain model analysis method is to express the state of the circuit utilizing mathematical functions. The calculation process of the time-domain model is based on calculus instead of iteration, with a smaller amount

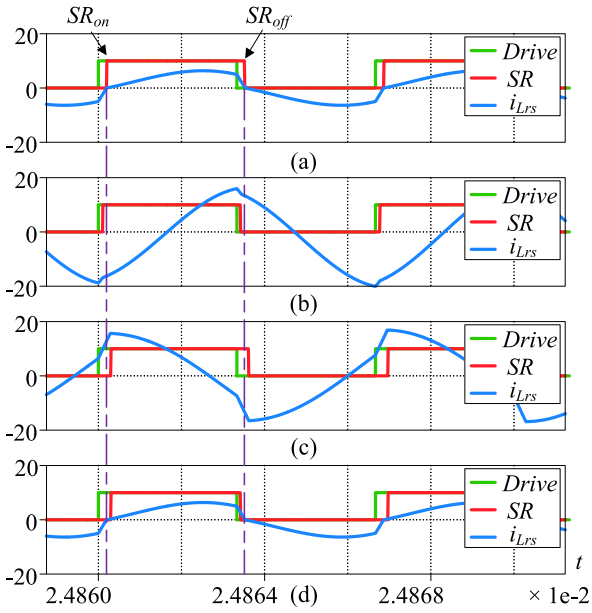

Fig. 7. Influence of the accuracy of the SR signal.

of calculation. However, in the resonant circuit, as the switching frequency changes, the resonant voltage and resonant current waveforms in a switching cycle are piecewise functions. In particular, the CLLC circuit contains many passive components, which cause problems such as multiple variables, high equation order, and complex algebra calculation in the time-domain model analysis process. These problems restrict the application of the time-domain model analysis method in the CLLC circuit. This article proposes a time-domain analysis method suitable for the resonant CLLC circuit. Decoupling calculations are used in the analysis and calculation of multiple variables. Accurate low-order function expressions are obtained as well. Similarly, the time-domain model is analyzed according to the relationship between the switching frequency and the resonant frequency. The secondary resonant current i_{Lrs} in the RFM is CRM, so this mode is used as the switching point of the other two modes and can be regarded as any other mode.

A. Time-Domain Model in URFM

As shown in Fig. 5, when the circuit works in URFM, the turn-ON period of the switches is less than the resonant period. The secondary resonant current i_{Lrs} is continuous, and the circuits on both sides of the transformer work together with one another. However, the voltage between C and D changes at the time t_{s0}, which is the zero-crossing point of i_{Lrs}. The simplified diagram of the CLLC circuit in this case can be expressed as Fig. 8.

Define the variable direction according to the symbol definition in Fig. 8. The input voltage v_1 and output voltage v_2 can be represented by Fig. 9, where $V_1 = V_P$, $V_2 = nV_S$ is the conversion results of V_S according to the transformer ratio n. It can be seen that there is a phase angle difference between v_1 and v_2. Correspondingly, the voltage and current waveforms are piecewise functions, as is shown in Fig. 5.

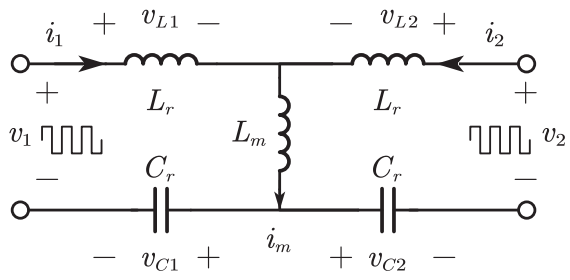

Fig. 8. Simplified CLLC circuit diagram.

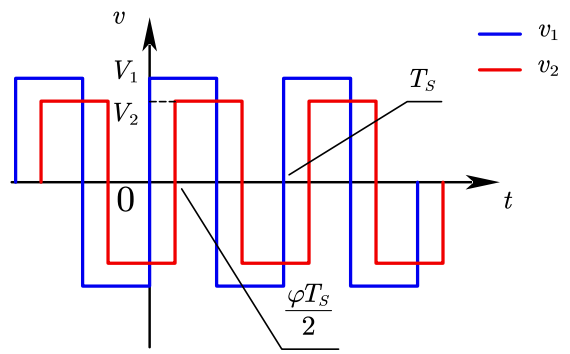

Fig. 9. Waveforms of input voltage v_1 and output voltage v_2.

The state equations of the voltage and current of passive components in Fig. 8 can be expressed by

$$\begin{cases} v_1 = L_r \frac{\mathrm{d}i_1}{\mathrm{d}t} + L_m \frac{\mathrm{d}(i_1+i_2)}{\mathrm{d}t} + v_{C1} \\ i_1 = C_r \frac{\mathrm{d}v_{C1}}{\mathrm{d}t} \\ v_2 = L_r \frac{\mathrm{d}i_2}{\mathrm{d}t} + L_m \frac{\mathrm{d}(i_1+i_2)}{\mathrm{d}t} + v_{C2} \\ i_2 = C_r \frac{\mathrm{d}v_{C2}}{\mathrm{d}t}. \end{cases} \tag{1}$$

In (1), v_1 and v_2 can be regarded as known conditions and the other four variables on the two sides of the transformer are coupled. Equation (1) is a second-order differential equation with four variables. It can be seen that the sum of i_1 and i_2 is the magnetizing current i_m. Taking the sum and difference for these variables, we can obtain

$$\begin{cases} v_1 - v_2 = L_r \frac{\mathrm{d}(i_1-i_2)}{\mathrm{d}t} + v_{C1} - v_{C2} \\ i_1 - i_2 = C_r \frac{\mathrm{d}(v_{C1}-v_{C2})}{\mathrm{d}t} \\ v_1 + v_2 = L_r \frac{\mathrm{d}(i_1+i_2)}{\mathrm{d}t} + 2L_m \frac{\mathrm{d}(i_1+i_2)}{\mathrm{d}t} + v_{C1} + v_{C2} \\ i_1 + i_2 = C_r \frac{\mathrm{d}(v_{C1}+v_{C2})}{\mathrm{d}t}. \end{cases} \tag{2}$$

Define d and s as difference and sum. According to (32) in Appendix, (2) can be expressed as follows:

$$\begin{cases} v_1 - v_2 = L_r \frac{\mathrm{d}i_d}{\mathrm{d}t} + v_{Cd} \\ i_d = C_r \frac{\mathrm{d}v_{Cd}}{\mathrm{d}t} \end{cases} \tag{3}$$

$$\begin{cases} v_1 + v_2 = (L_r + 2L_m) \frac{\mathrm{d}i_s}{\mathrm{d}t} + v_{Cs} \\ i_s = C_r \frac{\mathrm{d}v_{Cs}}{\mathrm{d}t}. \end{cases} \tag{4}$$

Equations (3) and (4) are simple second-order differential functions and are independent of each other. Equation (3) describes the change law of the difference, and (4) describes the change law of the sum. They are analyzed separately below.

Due to the half-wave symmetry, it is only necessary to analyze the working process within half switching cycle. At $\varphi T_s/2$, v_2 changes from $-V_2$ to V_2. Then, solve the differential (3) to get the general solution (5) as follows:

$$v_{Cd}(t) = \begin{cases} \alpha_1 \sin \omega_r t + \alpha_2 \cos \omega_r t + V_1 + V_2, & 0 < t < \varphi T_s/2 \\ \alpha_3 \sin \omega_r t + \alpha_4 \cos \omega_r t + V_1 - V_2, & \varphi T_s/2 < t < T_s/2 \end{cases} \tag{5}$$

where $\alpha_1 \sim \alpha_4$ are undetermined parameters, $f_n$is normalized resonant frequency, and $\omega_r$is resonant angle frequency. Their relationship is described as follows:

$$\begin{cases} \omega_r = \frac{1}{\sqrt{L_r C_r}} \\ \omega_r \cdot \frac{T_s}{2} = \frac{\pi}{f_n} \\ \omega_r \cdot \frac{\varphi T_s}{2} = \frac{\varphi \pi}{f_n}. \end{cases} \tag{6}$$

Differential of capacitor voltage has physical meaning of current, differentiating (5) we can obtain

$$\frac{1}{\omega_r} \cdot \frac{\mathrm{d}v_{Cd}(t)}{\mathrm{d}t} = \begin{cases} \alpha_1 \cos \omega_r t - \alpha_2 \sin \omega_r t & , \quad 0 < t < \frac{\varphi T_s}{2} \\ \alpha_3 \cos \omega_r t - \alpha_4 \sin \omega_r t & , \quad \frac{\varphi T_s}{2} < t < \frac{T_s}{2}. \end{cases} \tag{7}$$

Bring $v_{Cd}(0) + v_{Cd}(T_s/2) = 0$ into (5), according to the half-wave symmetry, we can obtain

$$\alpha_2 + \left(\sin \frac{\pi}{f_n}\right) \alpha_3 + \left(\cos \frac{\pi}{f_n}\right) \alpha_4 = -2V_1. \tag{8}$$

Simultaneously, (5) is continuous at time $t = \varphi T_s/2$, we can obtain

$$-2V_2 = \left(\sin \frac{\varphi\pi}{f_n}\right) \alpha_1 + \left(\cos \frac{\varphi\pi}{f_n}\right) \alpha_2 - \left(\sin \frac{\varphi\pi}{f_n}\right) \alpha_3 - \left(\cos \frac{\varphi\pi}{f_n}\right) \alpha_4. \tag{9}$$

Similarly, (7) also satisfies the half-wave symmetry and continuity conditions, which is expressed as

$$\alpha_1 + \left(\cos \frac{\pi}{f_n}\right) \alpha_3 - \left(\sin \frac{\pi}{f_n}\right) \alpha_4 = 0 \tag{10}$$

$$\left(\cos \frac{\varphi\pi}{f_n}\right) \alpha_1 - \left(\sin \frac{\varphi\pi}{f_n}\right) \alpha_2 - \left(\cos \frac{\varphi\pi}{f_n}\right) \alpha_3 + \left(\sin \frac{\varphi\pi}{f_n}\right) \alpha_4 = 0. \tag{11}$$

Combine (8)–(11), undetermined parameters can be expressed as

$$\begin{bmatrix} \alpha_1 \\ \alpha_2 \\ \alpha_3 \\ \alpha_4 \end{bmatrix} = \begin{bmatrix} -\frac{V_1 \sin \frac{\pi}{f_n} + V_2\left(\sin \frac{(\varphi-1)\pi}{f_n} + \sin \frac{\varphi\pi}{f_n}\right)}{\cos \frac{\pi}{f_n} + 1} \\ -\frac{V_1\left(1 + \cos \frac{\pi}{f_n}\right) + V_2\left(\cos \frac{(\varphi-1)\pi}{f_n} + \cos \frac{\varphi\pi}{f_n}\right)}{\cos \frac{\pi}{f_n} + 1} \\ \frac{-V_1 \sin \frac{\pi}{f_n} + V_2\left(\sin \frac{(\varphi+1)\pi}{f_n} + \sin \frac{\varphi\pi}{f_n}\right)}{\cos \frac{\pi}{f_n} + 1} \\ -\frac{V_1\left(1 + \cos \frac{\pi}{f_n}\right) - V_2\left(\cos \frac{(\varphi+1)\pi}{f_n} + \cos \frac{\varphi\pi}{f_n}\right)}{\cos \frac{\pi}{f_n} + 1} \end{bmatrix}. \tag{12}$$

Similarly, consider the change law of the sum (4), general solution (13) can be obtained as

$$v_{Cs}(t) = \begin{cases} \beta_1 \sin\omega_m t + \beta_2 \cos\omega_m t + V_1 - V_2 \ , \ 0 < t < \varphi T_s/2 \\ \beta_3 \sin\omega_m t + \beta_4 \cos\omega_m t + V_1 + V_2 \ , \ \varphi T_s/2 < t < T_s/2 \end{cases} \tag{13}$$

where $\beta_1 \sim \beta_4$ are undetermined parameters, f_m and ω_m are normalized ratio. Their relationship is as follows:

$$\begin{cases} f_m = f_s \cdot 2\pi\sqrt{(2L_m + L_r)\, C_r} \\ \omega_m \cdot \frac{T_s}{2} = \frac{\pi}{f_m} \\ \omega_m \cdot \frac{\varphi T_s}{2} = \frac{\varphi\pi}{f_m}. \end{cases} \tag{14}$$

Special solution parameters matrix (15) can be obtained according to half-wave symmetry and continuity, which is as follows:

$$\begin{bmatrix} \beta_1 \\ \beta_2 \\ \beta_3 \\ \beta_4 \end{bmatrix} = \begin{bmatrix} \frac{-V_1 \sin\frac{\pi}{f_m} + V_2\left(\sin\frac{(\varphi-1)\pi}{f_m} + \sin\frac{\varphi\pi}{f_m}\right)}{\cos\frac{\pi}{f_m} + 1} \\ -\frac{V_1\left(1+\cos\frac{\pi}{f_m}\right) - V_2\left(\cos\frac{(\varphi-1)\pi}{f_m} + \cos\frac{\varphi\pi}{f_m}\right)}{\cos\frac{\pi}{f_m} + 1} \\ -\frac{V_1 \sin\frac{\pi}{f_m} + V_2\left(\sin\frac{(\varphi+1)\pi}{f_m} + \sin\frac{\varphi\pi}{f_m}\right)}{\cos\frac{\pi}{f_m} + 1} \\ -\frac{V_1\left(1+\cos\frac{\pi}{f_m}\right) + V_2\left(\cos\frac{(\varphi+1)\pi}{f_m} + \cos\frac{\varphi\pi}{f_m}\right)}{\cos\frac{\pi}{f_m} + 1} \end{bmatrix}. \tag{15}$$

The time-domain expression (16) of the secondary side resonant current i_2 can be obtained by (1), (2), (5), (13), and (32) in Appendix, which is as follows:

$$i_2 = \begin{cases} \frac{C_r}{2}\begin{pmatrix} -\alpha_1\omega_r\cos\omega_r t + \alpha_2\omega_r\sin\omega_r t \\ +\beta_1\omega_m\cos\omega_m t - \beta_2\omega_m\sin\omega_m t \end{pmatrix}, & 0<t<\frac{\varphi T_s}{2} \\ \frac{C_r}{2}\begin{pmatrix} -\alpha_3\omega_r\cos\omega_r t + \alpha_4\omega_r\sin\omega_r t \\ +\beta_3\omega_m\cos\omega_m t - \beta_4\omega_m\sin\omega_m t \end{pmatrix}, & \frac{\varphi T_s}{2}<t<\frac{T_s}{2} \end{cases} \tag{16}$$

where the parameters $\alpha_1 \sim \alpha_4$ and $\beta_1 \sim \beta_4$ satisfy the relationship in (12) and (15).

In conclusion, the time-domain expression of the resonant CLLC circuit in URFM has been calculated. The current i_2 crosses zero at t_{s0}. Therefore, when the resonant network parameters, input and output voltages, and switching frequency (transmission power) are known, SR angle φ can be solved by (16).

B. Time-Domain Model in LRFM

As shown in Fig. 2, when the circuit works in LRFM, the turn-ON period of the switches is more than the resonant period, and the secondary resonant current i_{Lrs} is discontinuous. According to the value of i_{Lrs}, the half switching cycle can be divided into two parts, *Stages a* and *b*.

1) *Stage a*: Since i_{Lrs} is continuous, simplified CLLC circuit diagram under this state is the same as URFM, which is shown in Fig. 8. However, the voltage between two points C and D is constant V_S. Same with the previous calculation method, (33) and (34) can be easily obtained in Appendix, where $A_{a1} \sim A_{a4}$ are undetermined parameters.
2) *Stage b*: For i_{Lrs} remains zero, the current situation in the circuit can be represented by Fig. 3(d). In this stage, the two sides of the transformer work separately, and the circuit diagram can be simplified to Fig. 10.

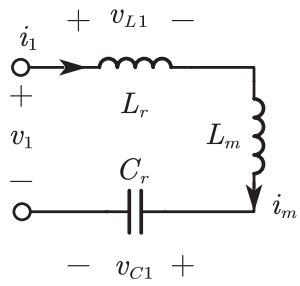

Fig. 10. Simplified CLLC circuit diagram in *Stage b*.

According to Fig. 10, list the differential equations at this stage, we can obtain

$$\begin{cases} v_1 = (L_r + L_m)\frac{\mathrm{d}i_1(t)}{\mathrm{d}t} + v_{C1}(t) \\ i_1(t) = i_m(t) = C_r\frac{\mathrm{d}v_{C1}(t)}{\mathrm{d}t}. \end{cases} \tag{17}$$

Equation (17) is a simple second-order differential equation with two variables, solve (17) to get (35) in the Appendix. In (35), A_{b1} and A_{b2} are undetermined parameters, φ and ω_b are represented by

$$\begin{cases} t_{s0} = \frac{(1-\varphi)T_s}{2} \\ \omega_b = \frac{1}{\sqrt{(L_m+L_r)C_r}}. \end{cases} \tag{18}$$

According to the analysis of *Stages a* and *b*, the general solution expression can be represented by (33) and (35) in Appendix. Sorting out the analysis and calculation results in *Stages a* and *B* in LRFM, the circuit state expression in LRFM can be obtained as

$$\begin{cases} i_{2.a}(0) = 0 \\ i_{2.a}\left(\frac{(1-\varphi)T_s}{2}\right) = 0 \\ i_{1.a}(0) + i_{1.b}\left(\frac{T_s}{2}\right) = 0 \\ i_{1.a}\left(\frac{(1-\varphi)T_s}{2}\right) = i_{1.b}\left(\frac{(1-\varphi)T_s}{2}\right) \\ v_{C1.a}\left(\frac{(1-\varphi)T_s}{2}\right) = v_{C1.b}\left(\frac{(1-\varphi)T_s}{2}\right) \\ v_{C2}(0) + v_{C2}\left(\frac{T_s}{2}\right) = v_{C2.a}(0) + v_{C2.a}\left(\frac{(1-\varphi)T_s}{2}\right) = 0 \\ v_{C1.a}(0) + v_{C1.b}\left(\frac{T_s}{2}\right) = 0. \end{cases} \tag{19}$$

Bring the time state into (19) to get (20), which is the system of equations to solve the parameters

$$\begin{cases} \omega_{a1}A_{a2}-\omega_{a2}A_{a4}=0 \\ \omega_{a1}\left[-A_{a1}\sin\left(\omega_{a1}\frac{(1-\varphi)T_s}{2}\right)+A_{a2}\cos\left(\omega_{a1}\frac{(1-\varphi)T_s}{2}\right)\right] \\ \quad +\omega_{a2}\left[A_{a3}\sin\left(\omega_{a2}\frac{(1-\varphi)T_s}{2}\right)-A_{a4}\cos\left(\omega_{a2}\frac{(1-\varphi)T_s}{2}\right)\right]=0 \\ \omega_{a1}A_{a2}+\omega_{a2}A_{a4}-\omega_bA_{b1}\sin\left(\omega_b\frac{\varphi T_s}{2}\right)+\omega_bA_{b2}\cos \\ \left(\omega_b\frac{\varphi T_s}{2}\right)=0 \\ \omega_{a1}\left[-A_{a1}\sin\left(\omega_{a1}\frac{(1-\varphi)T_s}{2}\right)+A_{a2}\cos\left(\omega_{a1}\frac{(1-\varphi)T_s}{2}\right)\right] \\ \quad +\omega_{a2}\left[-A_{a3}\sin\left(\omega_{a2}\frac{(1-\varphi)T_s}{2}\right)+A_{a4}\cos\left(\omega_{a2}\frac{(1-\varphi)T_s}{2}\right)\right] \\ =\omega_bA_{b2} \\ A_{a1}\cos\left(\omega_{a1}\frac{(1-\varphi)T_s}{2}\right)+A_{a2}\sin\left(\omega_{a1}\frac{(1-\varphi)T_s}{2}\right) \\ \quad +A_{a3}\cos\left(\omega_{a2}\frac{(1-\varphi)T_s}{2}\right)+A_{a4}\sin\left(\omega_{a2}\frac{(1-\varphi)T_s}{2}\right)=A_{b1} \\ A_{a1}-A_{a3}-V_2+A_{a1}\cos\left(\omega_{a1}\frac{(1-\varphi)T_s}{2}\right) \\ +A_{a2}\sin\left(\omega_{a1}\frac{(1-\varphi)T_s}{2}\right)-A_{a3}\cos\left(\omega_{a2}\frac{(1-\varphi)T_s}{2}\right) \\ \quad -A_{a4}\sin\left(\omega_{a2}\frac{(1-\varphi)T_s}{2}\right)-V_2=0 \\ A_{a1}+A_{a3}+V_1+A_{b1}\cos\left(\omega_b\frac{\varphi T_s}{2}\right) \\ +A_{b2}\sin\left(\omega_b\frac{\varphi T_s}{2}\right)+V_1=0. \end{cases} \tag{20}$$

In (20), the switching period T_S, the input voltage V_1, and the output voltage V_2 are known quantities of the current state of the circuit. There are other seven parameters A_{a1}, A_{a2}, A_{a3}, A_{a4}, A_{b1}, A_{b2}, and φ. We obtain the following, from (20), as the final φ value calculation expression:

$$\begin{aligned} &\omega_{a1}\left[-A_{a1}\sin\left(\omega_{a1}\frac{(1-\varphi)T_s}{2}\right)+A_{a2}\cos\left(\omega_{a1}\frac{(1-\varphi)T_s}{2}\right)\right] \\ &+\omega_{a2}\left[-A_{a3}\sin\left(\omega_{a2}\frac{(1-\varphi)T_s}{2}\right)+A_{a4}\cos\left(\omega_{a2}\frac{(1-\varphi)T_s}{2}\right)\right] \\ &=\omega_bA_{b2}. \end{aligned} \tag{21}$$

Simplify the other expressions in (20), so that A_{a1}, A_{a2}, A_{a3}, A_{a4}, A_{b1}, and A_{b2} can be expressed by φ. The expressions of the parameters in (21) can be listed as shown in (36) in Appendix.

In summary, by bringing the switching period T_S, the input voltage V_1 and the output voltage V_2 into (21), the SR angle φ in a certain state can be obtained.

C. Robustness of the Proposed Modeling

Sensitivity is generally used to indicate the degree of change of a variable affected by other variables. The SR angle φ between the primary drive signal and secondary resonant inductor current is numerically calculated from (22) in URFM and (23) in LRFM. The corresponding sensitivity can be obtained by considering the parameter of (22) or (23) that need to be analyzed for sensitivity as a variable and performing partial differential calculation of (22) and (23). The expression of LRFM is more complicated, so the calculation process of partial differential is difficult to show in the article. And parameter sensitivity analysis requires the assistance of mathematical analysis tools such as MATLAB. The parameter sensitivity analysis in the case of LRFM is omitted. The following shows the sensitivity analysis of parameter in URFM

$$\begin{aligned} &i_2\left(\frac{\varphi T_s}{2}\right) \\ &=\frac{C_r}{2}\begin{pmatrix}-\alpha_1\omega_r\cos\omega_r\frac{\varphi T_s}{2}+\alpha_2\omega_r\sin\omega_r\frac{\varphi T_s}{2} \\ +\beta_1\omega_m\cos\omega_m\frac{\varphi T_s}{2}-\beta_2\omega_m\sin\omega_m\frac{\varphi T_s}{2}\end{pmatrix}=0 \end{aligned} \tag{22}$$

$$\begin{aligned} &\omega_{a1}\left[-A_{a1}\sin\left(\omega_{a1}\frac{(1-\varphi)T_s}{2}\right)+A_{a2}\cos\left(\omega_{a1}\frac{(1-\varphi)T_s}{2}\right)\right] \\ &+\omega_{a2}\left[-A_{a3}\sin\left(\omega_{a2}\frac{(1-\varphi)T_s}{2}\right)+A_{a4}\cos\left(\omega_{a2}\frac{(1-\varphi)T_s}{2}\right)\right] \\ &=\omega_bA_{b2}. \end{aligned} \tag{23}$$

Equation (22) can be rewritten as an implicit function of φ and L_r as

$$\begin{aligned} &F\left(\varphi,L_r\right) \\ &=\frac{C_r}{2}\begin{pmatrix}-\alpha_1\omega_r\cos\omega_r\frac{\varphi T_s}{2}+\alpha_2\omega_r\sin\omega_r\frac{\varphi T_s}{2} \\ +\beta_1\omega_m\cos\omega_m\frac{\varphi T_s}{2}-\beta_2\omega_m\sin\omega_m\frac{\varphi T_s}{2}\end{pmatrix}=0. \end{aligned} \tag{24}$$

According to the definition of parameter sensitivity, $S_{L_r}^{\varphi}$ represents the degree of influence on φ when L_r changes, and its expression is as

$$S_{L_r}^{\varphi}=\frac{d\varphi/\varphi}{dL_r/L_r}. \tag{25}$$

Calculate (24) according to the implicit function derivation rule to get

$$\frac{d\varphi}{dL_r}=-\frac{\partial F}{\partial L_r}/\frac{\partial F}{\partial\varphi}. \tag{26}$$

Decompose $F(\varphi,L_r)$ in (24) into $F_{1\sim4}$, as shown in Appendix, to facilitate subsequent calculations, where $C_r/2$ is not equal to 0 can be omitted

$$\frac{d\varphi}{dL_r}=-\frac{\frac{\partial F_1}{\partial L_r}+\frac{\partial F_2}{\partial L_r}+\frac{\partial F_3}{\partial L_r}+\frac{\partial F_4}{\partial L_r}}{\frac{\partial F_1}{\partial\varphi}+\frac{\partial F_2}{\partial\varphi}+\frac{\partial F_3}{\partial\varphi}+\frac{\partial F_4}{\partial\varphi}}. \tag{27}$$

As shown in (27), there are eight partial differential calculations. The calculation process of $\partial F_1/\partial L_r$ is shown in (28) as an example, and the rest are shown in Appendix

$$\begin{aligned} \frac{\partial F_1}{\partial L_r}&=-\frac{\partial\alpha_1}{\partial L_r}\omega_r\cos\left(\frac{\varphi}{2}T_s\omega_r\right)-\frac{\partial\omega_r}{\partial L_r}\alpha_1\cos\left(\frac{\varphi}{2}T_s\omega_r\right) \\ &\quad-\frac{\partial\left[\cos\left(\frac{\varphi}{2}T_s\omega_r\right)\right]}{\partial L_r}\alpha_1\omega_r \\ &=-\frac{\partial\alpha_1}{\partial L_r}\omega_r\cos\left(\frac{\varphi}{2}T_s\omega_r\right)-\frac{\partial\omega_r}{\partial L_r}\alpha_1\cos\left(\frac{\varphi}{2}T_s\omega_r\right) \\ &\quad+\frac{\partial\omega_r}{\partial L_r}\frac{\varphi}{2}T_s\alpha_1\omega_r\sin\left(\frac{\varphi}{2}T_s\omega_r\right). \end{aligned} \tag{28}$$

There are two new partial derivative expressions $\partial\alpha_1/\partial L_r$ and $\partial\omega_r/\partial L_r$ in (28), and they can be represented by

$$\begin{cases} \frac{\partial\alpha_1}{\partial L_r}=C_rT_s\times\left\{\frac{V_1\cos\frac{\pi}{f_n}+V_2\left[\varphi\cos\frac{\varphi\pi}{f_n}+(\varphi-1)\cos\frac{(\varphi-1)\pi}{f_n}\right]}{4\left(1+\cos\frac{\pi}{f_n}\right)(L_rC_r)^{\frac{3}{2}}}\right. \\ \left.+\frac{\sin\frac{\pi}{f_n}\times\left[V_1\sin\frac{\pi}{f_n}+V_2\sin\frac{\varphi\pi}{f_n}+V_2\sin\frac{(\varphi-1)\pi}{f_n}\right)\right]}{4\left(1+\cos\frac{\pi}{f_n}\right)^2(L_rC_r)^{\frac{3}{2}}}\right\} \\ \frac{\partial\omega_r}{\partial L_r}=-\frac{C_r}{2(L_rC_r)^{3/2}}. \end{cases} \tag{29}$$

TABLE III
ESTIMATION INACCURACY WITH RESONANT INDUCTOR VARIATIONS

% variation in L_r	Estimation inaccuracy (%)
0% (no change)	0%
5%	1.34%
10%	2.65%
20%	5.13%

TABLE IV
ESTIMATION INACCURACY WITH RESONANT CAPACITOR VARIATIONS

% variation in C_r	Estimation inaccuracy (%)
0% (no change)	0%
5%	1.79%
10%	3.50%
20%	6.63%

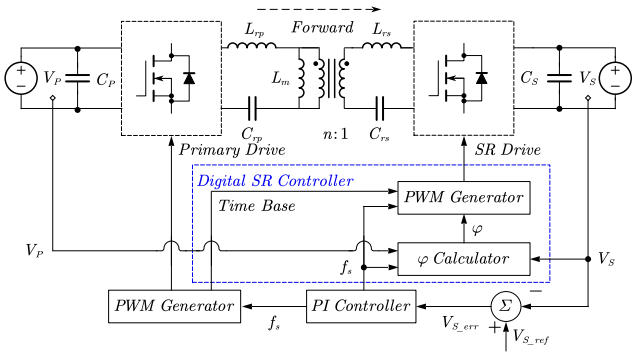

Fig. 11. Overall diagram of the proposed digital SR scheme.

Other expressions in (27) can also use similar calculation methods to get the final result. Put the calculation results of these partial derivative expressions into (26) to get the sensitivity of SR angle φ relative to parameter L_r. Table III shows the influence of the deviation of the resonant inductor L_r on the SR angle φ under the rated power transmission condition.

It can be seen from Table III that when L_r changes, the deviation of SR angle φ calculated by the proposed time-domain model is within the acceptable range. Similarly, the sensitivity of SR angle φ relative to parameter C_r can be calculated using formula (30), and the results of the deviation analysis are shown in Table IV. The deviation of SR angle φ caused by the change of the resonant capacitor C_r is also within the acceptable range

$$S_{C_r}^{\varphi} = \frac{d\varphi/\varphi}{dC_r/C_r}. \tag{30}$$

IV. DIGITAL SR SCHEME

Fig. 11 shows the overall diagram of the proposed digital SR scheme. When the CLLC circuit works in forward working mode, the PI controller calculates the switching frequency f_s according to the error of the output voltage V_S, and the PWM generator generates the primary drive signal according to the frequency information and the dead time. The generation method of the primary drive signal is consistent with the traditional control method of the CLLC circuit, and is not affected by the newly added digital SR control.

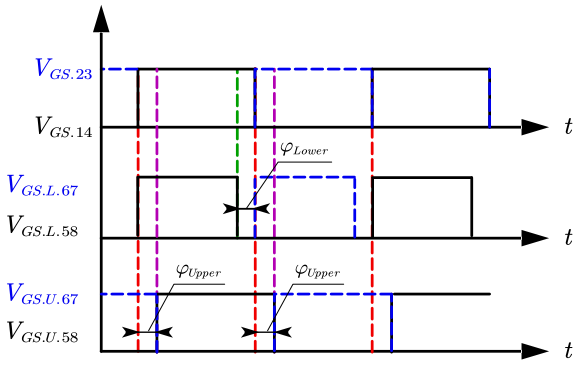

Fig. 12. Relationship between primary drive signals and SR signals in LRFM or URFM.

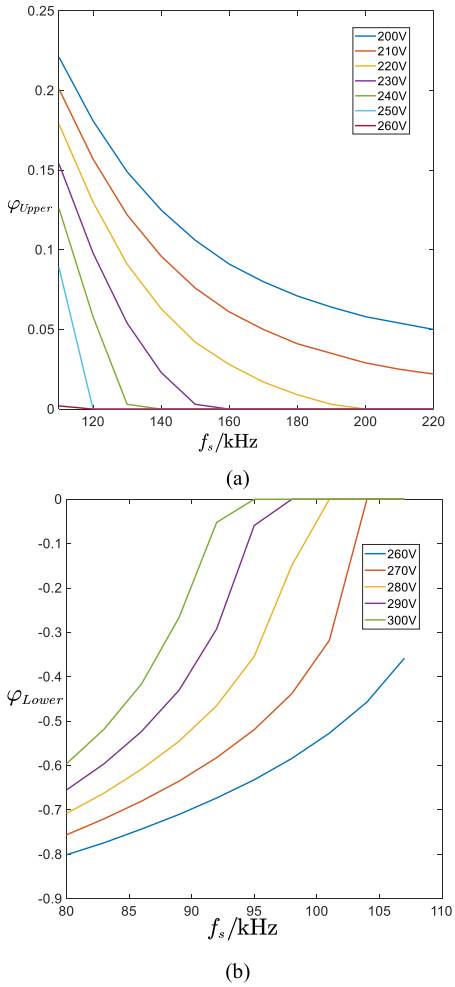

Fig. 13. Results of SR angle φ with output voltage V_S and switching frequency. (a) LRFM. (b) URFM.

In the digital SR controller, three variables of input voltage V_P, output voltage V_S, and switching frequency f_s are used to calculate the current working state of the CLLC circuit. The φ calculator carry out look-up table linearization analysis according to the circuit state to generate the SR angle φ. V_P and V_S can be obtained with the original dc voltage detection

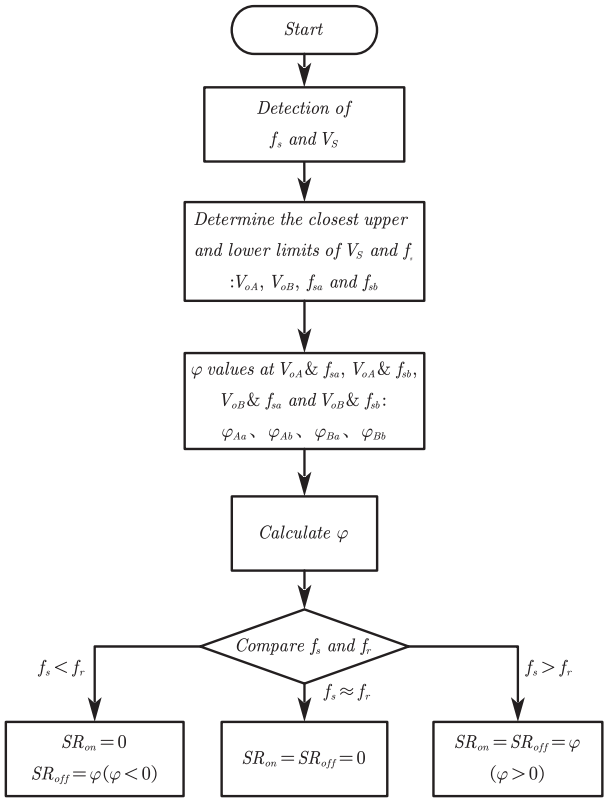

Fig. 14. Process of generating SR signals.

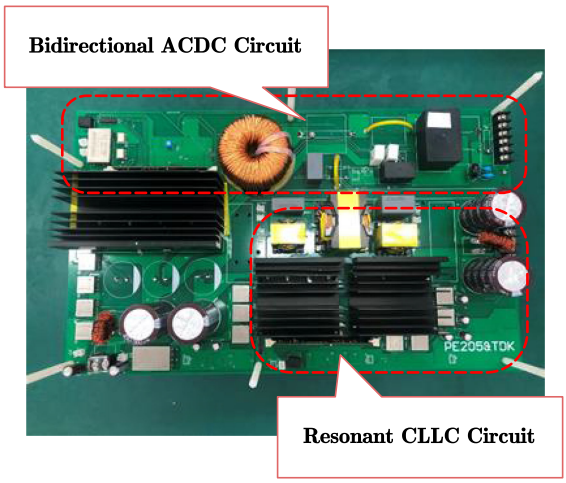

Fig. 15. Photograph of the prototype.

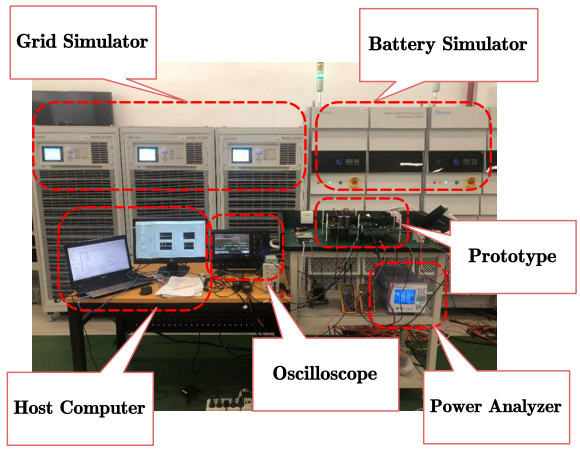

Fig. 16. Experimental test platform.

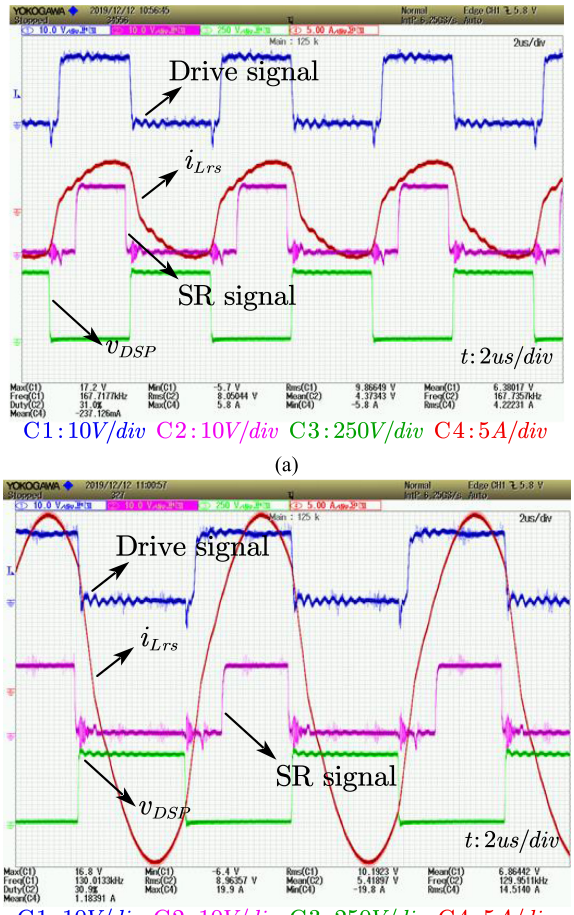

Fig. 17. Waveforms in URFM. (a) Light load. (b) Full load.

circuit. Since V_P and V_S are relatively stable dc voltage values, their sampling delay can be ignored. And f_s is the calculation result of the PI controller, which has no sampling delay. Finally, the SR PWM generator generates the SR drive signal according to the switching frequency f_s, the SR angle φ, and the time base.

For load changes, SR control is suitable for all frequency conversion control ranges. But when the switching frequency reaches the preset maximum, that is, when the load is very light, the circuit enters the burst operating mode. When the circuit is in burst mode, the resonant inductor current of the secondary side cannot maintain the normal waveform, and the SR function will be disabled. Only when the circuit working mode re-enters the frequency conversion mode and continues for a certain period of time, the SR function will be restarted. This scheme avoids

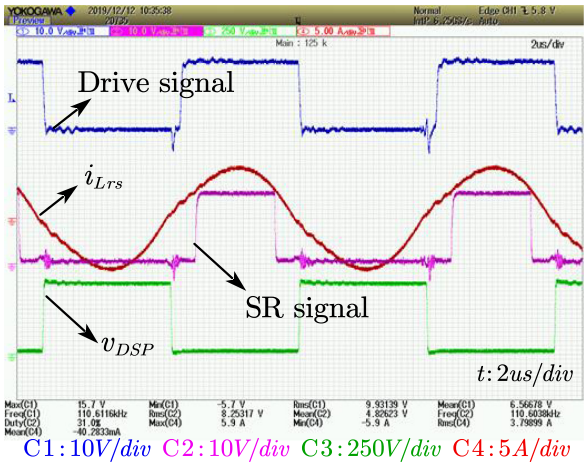

(a)

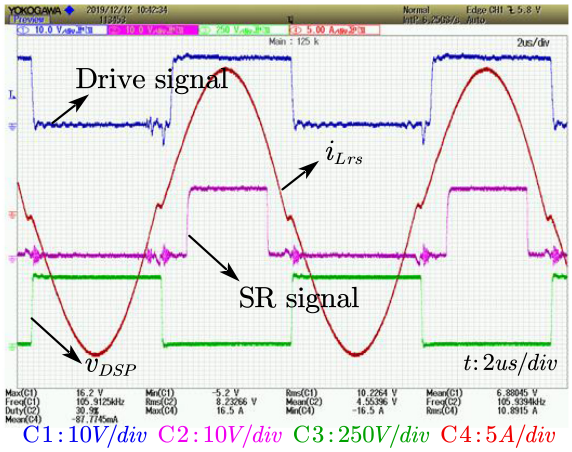

(b)

Fig. 18. Waveforms in RFM. (a) Light load. (b) Full load.

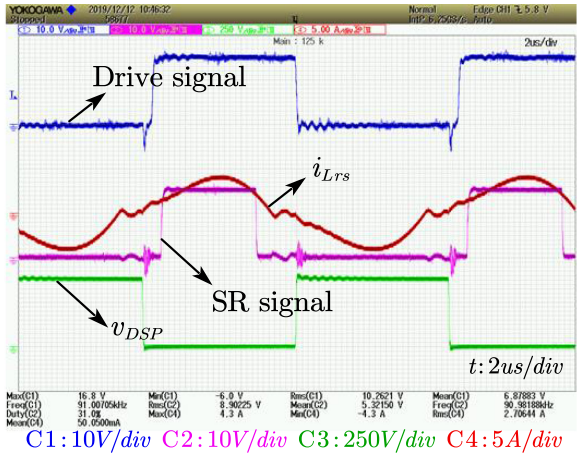

(a)

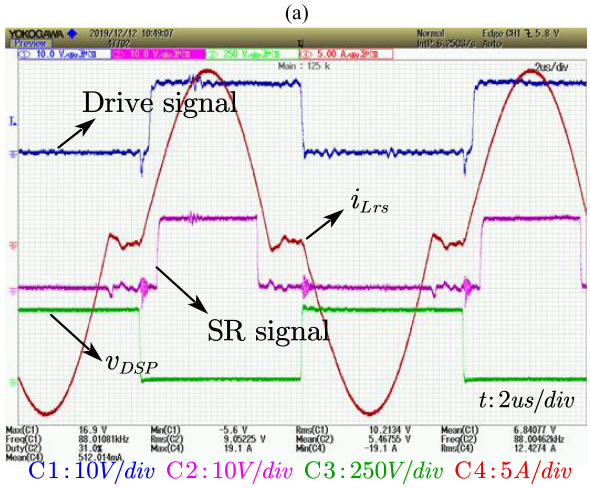

(b)

Fig. 19. Waveforms in LRFM. (a) Light load. (b) Full load.

frequently turning ON and OFF the SR function, and improves the stability of the CLLC circuit.

Through the time-domain model in Section III, the secondary side resonant current i_{Lrs} can be represented by functions. The moment when i_{Lrs} crosses zero is where the SR signal is triggered. The SR drive signals $V_{GS.L.n}$ in the LRFM and $V_{GS.U.n}$ in the URFM can be shown in Fig. 12, according to Figs. 2 and 5.

As shown in Fig. 12, $V_{GS.L.n}$ shows the SR signals in the LRFM. The turn-ON action of the SR signals can be simultaneous with the drive signals of the primary side, but the turn-OFF time will be ahead of φ_{Lower} angle relative to the drive signals. On the other hand, $V_{GS.U.n}$ indicates that the SR signals lag the primary drive signals by an angle φ_{Upper} in the URFM.

When the normalized switching angle frequency ω_n, quality factor Q, and voltage gain M of the resonant CLLC circuit are known, the state of the circuit is determined and unique. In other words, the value of two of these three states can determine the last. In FHA, Q and R_{eq} are inversely proportional, while Q is proportional to the transmission power P.

The SR angle φ of a resonant CLLC circuit in different working states can be obtained by bringing ω_n with the time-domain model calculated in Section III. In specific applications, when the resonant frequency f_r and input voltage V_P are determined, the switching frequency f_s and output voltage V_S can be used instead of ω_n and M.

Fig. 13 shows the change of SR angle φ with different f_s and V_S. Considering the computing power of the digital signal processor (DSP), the piecewise linearization method can be used to the SR signals generation on the DSP. The data in Fig. 13 can be stored in the DSP in the form of tables.

Fig. 14 shows the process of generating SR signals, definitions of SR_{on} and SR_{off} are the lag time of the SR signals turn-ON and turn-OFF, respectively, compared with the primary side drive signals. First, determine the closest state in the table based on the current circuit state. Then, the reference values of the SR angle φ are obtained in the table, and φ of the current state is calculated according to (31), which is as follows:

$$\begin{aligned}\varphi &= \varphi_A\left(\frac{V_o-V_{oA}}{V_{oB}-V_{oA}}\right)+\varphi_B\left(\frac{V_{oB}-V_o}{V_{oB}-V_{oA}}\right)\\ &=\left[\varphi_{Aa}\left(\frac{f_s-f_{sa}}{f_{sb}-f_{sa}}\right)+\varphi_{Ab}\left(\frac{f_{sb}-f_s}{f_{sb}-f_{sa}}\right)\right]\cdot\left(\frac{V_o-V_{oA}}{V_{oB}-V_{oA}}\right)\\ &\quad+\left[\varphi_{Ba}\left(\frac{f_s-f_{sa}}{f_{sb}-f_{sa}}\right)+\varphi_{Bb}\left(\frac{f_{sb}-f_s}{f_{sb}-f_{sa}}\right)\right]\cdot\left(\frac{V_{oB}-V_o}{V_{oB}-V_{oA}}\right).\end{aligned} \tag{31}$$

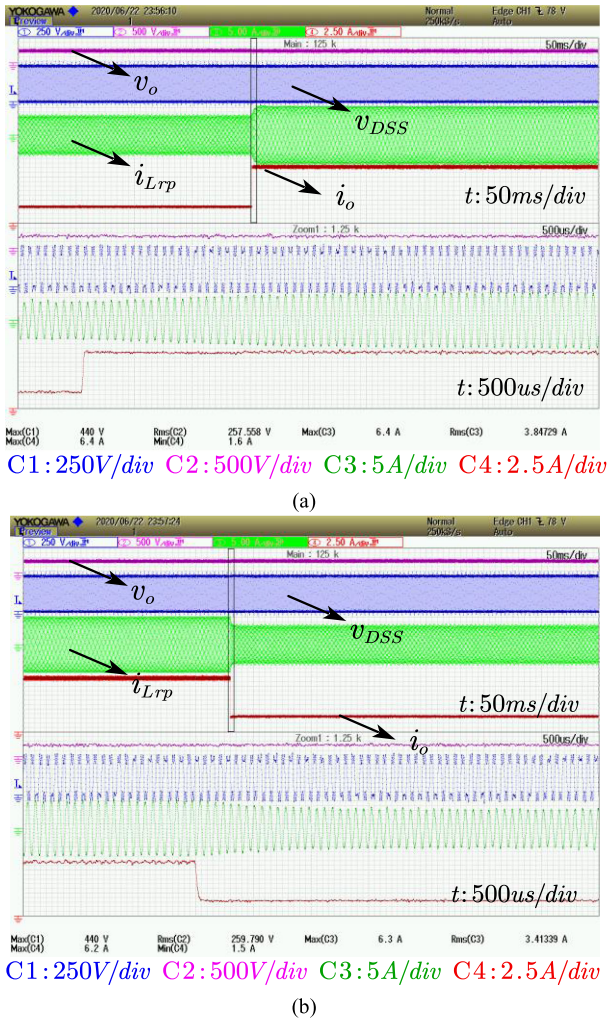

Fig. 20. Dynamic waveforms during load switching. (a) Increase load. (b) Reduce load.

Finally, the relationship between the switching frequency f_s and the resonant frequency f_r of the circuit is judged, and SR_{on} and SR_{off} of the SR signals are assigned. In particular, RFM is the transition state between LRFM and URFM. The values of SR_{on} and SR_{off} are both 0.

V. Experimental Verification

In order to verify the above-mentioned content, a prototype of a 3-kW resonant CLLC converter was set up. The key parameters of the prototype are shown in Table V. The prototype photo is shown in Fig. 15, a 3-kW bidirectional OBC, including two parts: a Totem-pole PFC and a resonant CLLC converter with the control chip TMS320F28335. The resonant inductor and high-frequency transformer use PC95 series PQ cores. The resonant capacitor material is the polypropylene film. Switches are SiC MOSFET of SCT3080AL. Finally, an experimental test platform, as shown in Fig. 16, is set up for related experiments.

Due to the passive components' parameter deviation and the influence of parasitic parameters in the switching devices and lines, an appropriate control margin is added to the calculated

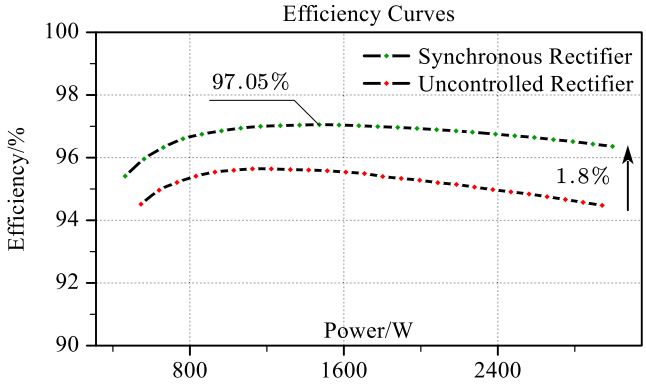

Fig. 21. Comparison of efficiency curves.

TABLE V
Key Parameters of CLLC Converter

Parameters	Values
Input Voltage	380V
Output Voltage (Rated)	200~300V (260V)
Resonant Frequency	110kHz
Rated Power	3kW
Transformer Ratio	19/13
Primary Resonant Inductor	22.57uH
Primary Resonant Capacitor	92.75nF
Secondary Resonant Inductor	10.57uH
Secondary Resonant Capacitor	198.12nF
Primary Magnetizing Inductor	79uH

secondary SR signals. This control margin ensures that the SR signals will not turn ON too early or turn OFF too late, avoiding problems such as circulating current. During the control margin period, the secondary resonant current i_{Lrs} is uncontrolled rectified through the MOSFETs' body diodes. Simultaneously, when the circuit is working in the dynamic switching process, a certain margin also ensures the circuit stability during the switching process. The current through the body diodes is small in this period, therefore no significant losses will occur.

Because the working state of the bidirectional resonant CLLC converter is related to the switching frequency, the digital SR scheme also uses the design of the segmented DSP programs. Figs. 17–19 show the oscilloscope waveforms of the circuit operating conditions in different working modes.

As shown in Fig. 17, in the URFM, it can be seen from the change of the resonant current i_{Lrs} that the SR signal on the secondary side should lag behind the primary-side variable-frequency control drive signal by a certain angle. As the load becomes heavy, the angle of lag will increase.

As shown in Fig. 18, in the RFM, it can be seen from the resonant current i_{Lrs} that the phase angle difference between the SR signal on the secondary side and the drive signal on the primary side is basically 0, and the deviation is small with the change of load.

As shown in Fig. 19, in the LRFM, it can be seen from the resonant current i_{Lrs} that the turn-ON time of the SR signal on the secondary side is close to the turn-ON time of the drive signal

of the primary switches. However, the turn-OFF time of the SR signal is ahead of the drive signal on the primary side by a certain angle. As the load increases, the angle enlarges as well.

As shown in Figs. 17–19, the proposed SR scheme can cover all the working states effectively.

Fig. 20 shows the dynamic waveforms during load switching. The primary resonant current i_{Lrp} and output current i_o change with load switching, while the output voltage v_o and the voltage across the secondary MOSFET v_{DSS} remain stable, which proves that the proposed SR scheme has excellent dynamic response capability.

From the above experimental waveforms, it can be seen that the secondary side SR signal has been maintained within a period when the secondary side resonant current i_{Lrs} is greater than 0. Moreover, the circuit working state is stable, which proves the accuracy and reliability of the proposed digital SR scheme.

During the experiment, the comparison of efficiency curves before and after using the proposed digital SR scheme was measured by the YOKOGAMA WT500 power analyzer, as shown in Fig. 21. The green dots and red dots, respectively, represent the efficiency measurement points of synchronous rectifier and uncontrolled rectifier. The efficiency performance of the converter is greatly improved with the application of the digital SR optimization strategy. The efficiency in the full power range has been improved, especially the full load efficiency has increased by 1.8%, and the efficiency reached a peak of 97.05% near half load. All the experimental results totally agree with the abovementioned analysis and calculation.

VI. Conclusion

In this article, different SR schemes and modeling methods of resonant circuit are discussed, and a novel modeling method based on time-domain analysis and an optimized digital SR control strategy are proposed. The time-domain modeling method proposed is an original method, which is more accurate than FHA, requires less computational effort than EHA, and is more convenient than simulation and artificial intelligence algorithm. Compared with other time-domain modeling methods, this article gives detailed circuit state expressions and covers the entire circuit operating states. Relying on the accurate circuit model, the SR scheme proposed in this article can adaptively generate SR signals in different frequency ranges and has the ability to switch modes smoothly. The proposed SR strategy achieves precise SR function without additional detection circuit, and saves volume and cost. And this method can be used for the later efficiency optimization of CLLC converters that do not originally have SR function, only through the control program update. Moreover, the influence of the inaccuracy of the SR drive signal is simulated and analyzed, and the deviation caused by the parameter resonant inductor L_r and the resonant capacitor C_r in the calculation process of the proposed SR angle φ is analyzed. Finally, the contents mentioned are verified by the experiment of a 3-kW CLLC converter. The comparison of efficiency curves proves that the proposed optimized digital SR control strategy effectively improves the efficiency of the CLLC converter, and the steady state and dynamic waveforms prove the reliability and stability of the scheme. The proposed modeling method and SR scheme are general for resonant CLLC topology, which can be widely applied in microgrid, electric vehicle, power electronic transformer, and so on.

Appendix

Define *d* and *s* as difference and sum, relationships among the input voltage v_1, input current i_1, output voltage v_2, and output current i_2 in Fig. 8 are as follows:

$$\begin{cases} i_d = i_1 - i_2 \\ v_{Cd} = v_{C1} - v_{C2} \\ i_s = i_m = i_1 + i_2 \\ v_{Cs} = v_{C1} + v_{C2}. \end{cases} \tag{32}$$

In LRFM, the half switching cycle can be divided into two parts, *Stages a* and *b*, according to the value of i_{Lrs}. In *Stage a*, the CLLC circuit working state of LRFM is similar to that of URFM, and the following formula can be obtained by a similar method in URFM, which is as follows:

$$\begin{cases} v_{C1.a}(t) = A_{a1}\cos(\omega_{a1}t) + A_{a2}\sin(\omega_{a1}t) \\ \quad + A_{a3}\cos(\omega_{a2}t) + A_{a4}\sin(\omega_{a2}t) + v_1 \\ v_{C2.a}(t) = -A_{a1}\cos(\omega_{a1}t) - A_{a2}\sin(\omega_{a1}t) \\ \quad + A_{a3}\cos(\omega_{a2}t) + A_{a4}\sin(\omega_{a2}t) + v_2 \\ i_{1.a}(t) = C_r\omega_{a1}\left[-A_{a1}\sin(\omega_{a1}t) + A_{a2}\cos(\omega_{a1}t)\right] \\ \quad + C_r\omega_{a2}\left[-A_{a3}\sin(\omega_{a2}t) + A_{a4}\cos(\omega_{a2}t)\right] \\ i_{2.a}(t) = C_r\omega_{a1}\left[A_{a1}\sin(\omega_{a1}t) - A_{a2}\cos(\omega_{a1}t)\right] \\ \quad + C_r\omega_{a2}\left[-A_{a3}\sin(\omega_{a2}t) + A_{a4}\cos(\omega_{a2}t)\right] \\ i_{m.a}(t) = 2C_r\omega_{a2}\left[-A_{a3}\sin(\omega_{a2}t) + A_{a4}\cos(\omega_{a2}t)\right] \end{cases} \tag{33}$$

$$\begin{cases} \omega_{a1} = \frac{1}{\sqrt{L_rC_r}} \\ \omega_{a2} = \frac{1}{\sqrt{(2L_m+L_r)C_r}}. \end{cases} \tag{34}$$

Solve the simple second-order differential equation in (17), the result Is

$$\begin{cases} v_{C1.b}(t) = A_{b1}\cos\left[\omega_b\left(t - \frac{(1-\varphi)T_s}{2}\right)\right] \\ \quad + A_{b2}\sin\left[\omega_b\left(t - \frac{(1-\varphi)T_s}{2}\right)\right] + v_1 \\ i_{1.b}(t) = -A_{b1}C_r\omega_b\sin\left[\omega_b\left(t - \frac{(1-\varphi)T_s}{2}\right)\right] \\ \quad + A_{b2}C_r\omega_b\cos\left[\omega_b\left(t - \frac{(1-\varphi)T_s}{2}\right)\right]. \end{cases} \tag{35}$$

The parameter expression of (21) is as follows:

$$\begin{cases} T_\varphi = \frac{\varphi T_s}{2}, T_c = \frac{(1-\varphi)T_s}{2} \\ A_{a1} = k_1A_{a2} + b_1 \\ A_{a2} = \frac{\omega_b[b_5\sin(\omega_bT_\varphi) - b_6\cos(\omega_bT_\varphi)]}{2\omega_{a1} - \omega_b[k_5\sin(\omega_bT_\varphi) - k_6\cos(\omega_bT_\varphi)]} \\ A_{a3} = k_3A_{a2} + b_3 \\ A_{a4} = \frac{\omega_{a1}}{\omega_{a2}}A_{a2} \\ A_{b1} = k_5A_{a2} + b_5 \\ A_{b2} = k_6A_{a2} + b_6. \end{cases} \tag{36}$$

In order to facilitate browsing, some parameters in (36) are replaced with *k* and *b*, as shown in (37).

Decompose $F(\varphi, L_r)$ in (24) into $F_{1\sim4}$, which are represented by

$$\begin{cases} k_1 = \frac{\omega_{a2}\sin(\omega_{a2}T_c)\left[\frac{\omega_{a1}}{\omega_{a2}}\sin(\omega_{a2}T_c)-\sin(\omega_{a1}T_c)\right]}{\omega_{a2}\sin(\omega_{a2}T_c)[1+\cos(\omega_{a1}T_c)]-\omega_{a1}\sin(\omega_{a1}T_c)[1+\cos(\omega_{a2}T_c)]} \\ \quad + \frac{\omega_{a1}[\cos(\omega_{a2}T_c)-\cos(\omega_{a1}T_c)][1+\cos(\omega_{a2}T_c)]}{\omega_{a2}\sin(\omega_{a2}T_c)[1+\cos(\omega_{a1}T_c)]-\omega_{a1}\sin(\omega_{a1}T_c)[1+\cos(\omega_{a2}T_c)]} \\ b_1 = \frac{2V_2\omega_{a2}\sin(\omega_{a2}T_c)}{[1+\cos(\omega_{a1}T_c)]\omega_{a2}\sin(\omega_{a2}T_c)-\omega_{a1}\sin(\omega_{a1}T_c)[1+\cos(\omega_{a2}T_c)]} \\ k_3 = k_1\frac{\omega_{a1}\sin(\omega_{a1}T_c)}{\omega_{a2}\sin(\omega_{a2}T_c)} + \frac{\omega_{a1}[\cos(\omega_{a2}T_c)-\cos(\omega_{a1}T_c)]}{\omega_{a2}\sin(\omega_{a2}T_c)} \\ b_3 = b_1\frac{\omega_{a1}\sin(\omega_{a1}T_c)}{\omega_{a2}\sin(\omega_{a2}T_c)} \\ k_5 = k_1\cos(\omega_{a1}T_c) + \sin(\omega_{a1}T_c) + k_3\cos(\omega_{a2}T_c) \\ \quad + \frac{\omega_{a1}}{\omega_{a2}}\sin(\omega_{a2}T_c) \\ b_5 = b_1\cos(\omega_{a1}T_c) + b_3\cos(\omega_{a2}T_c) \\ k_6 = -\frac{k_1+k_3+k_5\cos(\omega_bT_\varphi)}{\sin(\omega_bT_\varphi)} \\ b_6 = -\frac{b_1+b_3+b_5\cos(\omega_bT_\varphi)+2V_1}{\sin(\omega_bT_\varphi)} \end{cases} \tag{37}$$

$$\begin{cases} F_1(\varphi, L_r) = -\alpha_1\omega_{\rm r}\cos\left(\frac{\varphi T_s}{2}\omega_{\rm r}\right) \\ F_2(\varphi, L_r) = \alpha_2\omega_{\rm r}\sin\left(\frac{\varphi T_s}{2}\omega_{\rm r}\right) \\ F_3(\varphi, L_r) = \beta_1\omega_{\rm m}\cos\left(\frac{\varphi T_s}{2}\omega_{\rm m}\right) \\ F_4(\varphi, L_r) = -\beta_2\omega_{\rm m}\sin\left(\frac{\varphi T_s}{2}\omega_{\rm m}\right) \end{cases} \tag{38}$$

$$\begin{cases} \frac{\partial F_2}{\partial L_{\rm r}} = \frac{\partial\alpha_2}{\partial L_{\rm r}}\omega_r\sin\left(\frac{\varphi}{2}T_s\omega_r\right) + \frac{\partial\omega_r}{\partial L_{\rm r}}\alpha_2\sin\left(\frac{\varphi}{2}T_s\omega_r\right) + \\ \frac{\partial\omega_r}{\partial L_{\rm r}}\frac{\varphi}{2}T_s\alpha_2\omega_r\cos\left(\frac{\varphi}{2}T_s\omega_r\right) \\ \frac{\partial F_3}{\partial L_{\rm r}} = \frac{\partial\beta_1}{\partial L_{\rm r}}\omega_{\rm m}\cos\left(\frac{\varphi}{2}T_s\omega_m\right) + \frac{\partial\omega_m}{\partial L_{\rm r}}\beta_1\cos\left(\frac{\varphi}{2}T_s\omega_m\right) \\ -\frac{\partial\omega_m}{\partial L_{\rm r}}\frac{\varphi}{2}T_s\beta_1\omega_m\sin\left(\frac{\varphi}{2}T_s\omega_m\right) \\ \frac{\partial F_4}{\partial L_{\rm r}} = -\frac{\partial\beta_2}{\partial L_{\rm r}}\omega_{\rm m}\sin\left(\frac{\varphi}{2}T_s\omega_m\right) - \frac{\partial\omega_m}{\partial L_{\rm r}}\beta_2\sin\left(\frac{\varphi}{2}T_s\omega_m\right) \\ -\frac{\partial\omega_m}{\partial L_{\rm r}}\frac{\varphi}{2}T_s\beta_2\omega_m\cos\left(\frac{\varphi}{2}T_s\omega_m\right) \\ \frac{\partial F_1}{\partial\varphi} = -\frac{\partial\alpha_1}{\partial\varphi}\omega_r\cos\left(\frac{\varphi}{2}T_s\omega_r\right) + \frac{1}{2}T_s\omega_{\rm r}^2\alpha_1\sin\left(\frac{\varphi}{2}T_s\omega_r\right) \\ \frac{\partial F_2}{\partial\varphi} = \frac{\partial\alpha_2}{\partial\varphi}\omega_r\sin\left(\frac{\varphi}{2}T_s\omega_r\right) + \frac{1}{2}T_s\omega_r^2\alpha_2\cos\left(\frac{\varphi}{2}T_s\omega_r\right) \\ \frac{\partial F_3}{\partial\varphi} = \frac{\partial\beta_1}{\partial\varphi}\omega_{\rm m}\cos\left(\frac{\varphi}{2}T_s\omega_m\right) - \frac{1}{2}T_s\omega_m^2\beta_1\sin\left(\frac{\varphi}{2}T_s\omega_m\right) \\ \frac{\partial F_4}{\partial\varphi} = -\frac{\partial\beta_2}{\partial\varphi}\omega_{\rm m}\sin\left(\frac{\varphi}{2}T_s\omega_m\right) - \frac{1}{2}T_s\omega_m^2\beta_2\cos\left(\frac{\varphi}{2}T_s\omega_m\right). \end{cases} \tag{39}$$

The rest partial differential calculations in (27) are shown in (39).

ACKNOWLEDGMENT

The authors would like to thank TDK Inc. for providing materials and components for the research presented in this article and also PLEXIM Inc. for the support of the powerful simulation tools PLECS. They would like to thank Microgrid Electrical Equipment and Manufacture Platform (MEEMP) in the Polytechnic Institute of Zhejiang University, on which many valuable tests in this article were performed.

REFERENCES

[1] J. Huang, J. Xiao, C. Wen, P. Wang, and A. Zhang, "Implementation of bidirectional resonant DC transformer in hybrid AC/DC micro-grid," *IEEE Trans. Smart Grid*, vol. 10, no. 2, pp. 1532–1542, Mar. 2019.

[2] B. Li, Q. Li, F. C. Lee, Z. Liu, and Y. Yang, "A high-efficiency high-density wide-bandgap device-based bidirectional on-board charger," *IEEE J. Emerg. Sel. Topics Power Electron.*, vol. 6, no. 3, pp. 1627–1636, Sep. 2018.

[3] Y. Wang, B. Chen, Y. Hou, Z. Meng, and Y. Yang, "Analysis and design of a 1-MHz bidirectional multi-CLLC resonant DC–DC converter with GaN devices," *IEEE Trans. Ind. Electron.*, vol. 67, no. 2, pp. 1425–1434, Feb. 2020.

[4] J. Huang and X. Zhang, "Three-step switching frequency selection criteria for symmetrical CLLC-type DC transformer in hybrid AC/DC microgrid," *IEEE Trans. Power Electron.*, vol. 34, no. 10, pp. 9379–9385, Oct. 2019.

[5] N. Hou and Y. Li, "Overview and comparison of modulation and control strategies for non-resonant single-phase dual-active-bridge dc-dc converter," *IEEE Trans. Ind. Electron.*, vol. 35, no. 3, pp. 3148–3172, Mar. 2020.

[6] G. Pledl, M. Tauer, and D. Buecherl, "Theory of operation, design procedure and simulation of a bidirectional LLC resonant converter for vehicular applications," in *Proc. IEEE Veh. Power Propulsion Conf.*, Lille, 2010, pp. 1–5.

[7] B. Li, L. Jing, X. Wang, N. Chen, B. Liu, and M. Chen, "A smooth mode-switching strategy for bidirectional OBC base on V2G technology," in *Proc. IEEE Appl. Power Electron. Conf. Expo.*, Anaheim, CA, USA, 2019, pp. 3320–3324.

[8] N. Chen *et al.*, "A synchronous rectification scheme based on inductor voltage sensing for CLLC bidirectional resonant converter," in *Proc. IEEE Appl. Power Electron. Conf. Expo.*, New Orleans, LA, USA, 2020, pp. 1713–1719.

[9] S. Shao, H. Chen, X. Wu, J. Zhang, and K. Sheng, "Circulating current and ZVS-on of a dual active bridge DC-DC converter: A review," *IEEE Access*, vol. 7, pp. 50561–50572, 2019.

[10] Y. P. Chan, M. Yaqoob, C. S. Wong, and K. H. Loo, "Realization of high-efficiency dual-active-bridge converter with reconfigurable multi-level modulation scheme," *IEEE J. Emerg. Sel. Topics Power Electron.*, vol. 8, no. 2, pp. 1178–1192, Jun. 2020.

[11] J. Huang, Y. Wang, Z. Li, and W. Lei, "Unified triple-phase-shift control to minimize current stress and achieve full soft-switching of isolated bidirectional DC–DC converter," *IEEE Trans. Ind. Electron.*, vol. 63, no. 7, pp. 4169–4179, Jul. 2016.

[12] F. Wu, F. Feng, and H. B. Gooi, "Cooperative triple-phase-shift control for isolated DAB DC–DC converter to improve current characteristics," *IEEE Trans. Ind. Electron.*, vol. 66, no. 9, pp. 7022–7031, Sep. 2019.

[13] B. Zhao, Q. Song, W. Liu, and Y. Sun, "Overview of dual-active-bridge isolated bidirectional DC–DC converter for high-frequency-link power-conversion system," *IEEE Trans. Power Electron.*, vol. 29, no. 8, pp. 4091–4106, Aug. 2014.

[14] P. He and A. Khaligh, "Comprehensive analyses and comparison of 1 kW isolated DC–DC converters for bidirectional EV charging systems," *IEEE Trans. Transp. Electrific.*, vol. 3, no. 1, pp. 147–156, Mar. 2017.

[15] H. Li, Z. Zhang, S. Wang, J. Tang, X. Ren, and Q. Chen, "A 300-kHz 6.6-kW SiC bidirectional LLC onboard charger," *IEEE Trans. Ind. Electron.*, vol. 67, no. 2, pp. 1435–1445, Feb. 2020.

[16] G. Pledl, M. Tauer, and D. Buecherl, "Theory of operation, design procedure and simulation of a bidirectional LLC resonant converter for vehicular applications," in *Proc. IEEE Veh. Power Propulsion Conf.*, Lille, 2010, pp. 1–5.

[17] W. Chen, P. Rong, and Z. Lu, "Snubberless bidirectional DC–DC converter with new CLLC resonant tank featuring minimized switching loss," *IEEE Trans. Ind. Electron.*, vol. 57, no. 9, pp. 3075–3086, Sep. 2010.

[18] J. Jung, H. Kim, M. Ryu, and J. Baek, "Design methodology of bidirectional CLLC resonant converter for high-frequency isolation of DC distribution systems," *IEEE Trans. Power Electron.*, vol. 28, no. 4, pp. 1741–1755, Apr. 2013.

[19] P. He and A. Khaligh, "Design of 1 kW bidirectional half-bridge CLLC converter for electric vehicle charging systems," in *Proc. IEEE Int. Conf. Power Electron., Drives Energy Syst.*, Trivandrum, India, 2016, pp. 1–6.

[20] Z. U. Zahid, Z. M. Dalala, R. Chen, B. Chen, and J. Lai, "Design of bidirectional DC–DC resonant converter for vehicle-to-grid (V2G) applications," *IEEE Trans. Transp. Electrific.*, vol. 1, no. 3, pp. 232–244, Oct. 2015.

[21] Y. Tang, J. Lu, B. Wu, S. Zou, W. Ding, and A. Khaligh, "An integrated dual-output isolated converter for plug-in electric vehicles," *IEEE Trans. Veh. Technol.*, vol. 67, no. 2, pp. 966–976, Feb. 2018.

[22] D. Wang and Y. Liu, "A zero-crossing noise filter for driving synchronous rectifiers of LLC resonant converter," *IEEE Trans. Power Electron.*, vol. 29, no. 4, pp. 1953–1965, Apr. 2014.

[23] X. Xie, J. C. P. Liu, F. N. K. Poon, and M. H. Pong, "A novel high frequency current-driven synchronous rectifier applicable to most switching topologies," *IEEE Trans. Power Electron.*, vol. 16, no. 5, pp. 635–648, Sep. 2001.

[24] Y. Gao, K. Sun, X. Lin, and Z. Guo, "A phase-shift-based synchronous rectification scheme for bi-directional high-step-down CLLC resonant converters," in *Proc. IEEE Appl. Power Electron. Conf. Expo.*, San Antonio, TX, USA, 2018, pp. 1571–1576.
[25] S. Zou, J. Lu, A. Mallik, and A. Khaligh, "Bi-Directional CLLC converter with synchronous rectification for plug-in electric vehicles," *IEEE Trans. Ind. Appl.*, vol. 54, no. 2, pp. 998–1005, Mar./Apr. 2018.
[26] A. Sankar, A. Mallik, and A. Khaligh, "Extended harmonics based phase tracking for synchronous rectification in CLLC converters," *IEEE Trans. Ind. Electron.*, vol. 66, no. 8, pp. 6592–6603, Aug. 2019.
[27] W. Han and L. Corradini, "General closed-form ZVS analysis of dual-bridge series resonant DC–DC converters," *IEEE Trans. Power Electron.*, vol. 34, no. 9, pp. 9289–9302, Sep. 2019.
[28] B. Zhao, X. Zhang, and J. Huang, "AI algorithm-based two-stage optimal design methodology of high-efficiency CLLC resonant converters for the hybrid AC–DC microgrid applications," *IEEE Trans. Ind. Electron.*, vol. 66, no. 12, pp. 9756–9767, Dec. 2019.
[29] J. Sun, L. Yuan, Q. Gu, R. Duan, Z. Lu, and Z. Zhao, "Design-oriented comprehensive time-domain model for CLLC class isolated bidirectional DC-DC converter for various operation modes," *IEEE Trans. Power Electron.*, vol. 35, no. 4, pp. 3491–3505, Apr. 2020.

Bodong Li (Student Member, IEEE) received the B.S. degree in electrical engineering from Yanshan University, Qinhuangdao, China, in 2016, and the M.S. degree in electrical engineering in 2020 from Zhejiang University, Hangzhou, China where he is currently working toward the Ph.D. degree with the College of Electrical Engineering.

His research interests include high efficiency dc/dc converters, energy storage systems, photovoltaic, and microgrid systems.

Min Chen (Member, IEEE) received the B.S. degree in applied electronics and the Ph.D. degree in electrical engineering from Zhejiang University, Hangzhou, China, in 2000 and 2006, respectively.

From 2007 to 2009, he was a Postdoctoral Researcher with the Electrical Engineering Department, Zhejiang University, where he has been a Lecturer since 2010, and is currently an Associate Professor. From 2014 to 2015, he was a Visiting Researcher with the Department of Energy Technology, Aalborg University. Since 2007, he has been responsible for the Lighting Research and Development Laboratory, National Engineering Research Center for Applied Power Electronics. He has authored or coauthored more than 60 technical papers. He was also issued 14 patents of inventions. His research interests include power electronics in power system, inverter system, photovoltaic system and micro-inverter, electrical vehicle, regenerative energy system, distributed generation, energy storage system, modern lighting system for HID lamps and LED.

Xiaoqing Wang (Student Member, IEEE) received the B.S. degree in electrical engineering from China University of Mining and Technology, Xuzhou, China, in 2017. She is currently working toward the Ph.D. degree with the College of Electrical Engineering, Zhejiang University, Hangzhou, China.

Her research interests include energy storage systems, power decoupling, and high-efficiency ac/dc converters.

Ning Chen (Student Member, IEEE) received the B.S. degree in electrical engineering in 2018 from Zhejiang University, Hangzhou, China, where he is currently working toward the M.S. degree in electrical engineering.

His research interests include bidirectional dc/dc converters and resonant converters.

Xinnan Sun received the B.E. degree in electrical engineering in 2019 from Zhejiang University, Hangzhou, China, where she is currently working toward the Ph.D. degree with the College of Electrical Engineering.

Her research interests include bidirectional dc/dc converters and power modules.

Dongbo Zhang received the B.S. degree in electrical engineering in 2020 from Zhejiang University, Hangzhou, China, where he is currently working toward the M.S. degree in electrical engineering.

His research interests include wireless power transmission and high efficiency converters for renewable energy.